

Polarization-Insensitive Metalens with Extended Focal Depth and Longitudinal High-Tolerance Imaging

XiaoFei Zang, WeiWei Xu, Min Gu, BingShuang Yao, Lin Chen, Yan Peng, JingYa Xie, Alexey V. Balakin, Alexander P. Shkurinov, YiMing Zhu,* and SongLin Zhuang

Lenses with an extended focal depth have crucial applications in high-precision optical alignment systems and optical disk readout systems. However, further development of lenses with an extended focal depth under radial and angular modulation is limited because of fabrication difficulties. Metasurfaces, 2D metamaterials, have shown unprecedented capabilities in the manipulation of the intensity, phase, and polarization of electromagnetic waves. Here, based on geometric metasurfaces, an approach for realizing a terahertz metalens is proposed and experimentally demonstrated with simultaneous extended focal depth and polarization insensitivity. Under the illumination of arbitrarily polarized light, this metalens shows a focal depth of $\approx 23 \lambda$ along the propagation direction, resulting in an ultralong longitudinal working distance. As a proof-of-concept, longitudinal high-tolerance imaging based on the metalens is demonstrated. The unique approach for designing polarization-insensitive metalenses with an extended focal depth may find applications in imaging, lithography, and information processing.

lateral resolution^[1–3] and in presbyopia treatment.^[4,5] The reported approaches to realizing lenses with an extended focal depth, i.e., forward logarithmic axicons (FLAs), axilenses (AXLs), and light sword optical elements (LSOEs), are mainly based on radial modulation (RM) and angular modulation (AM).^[6] However, the phase profiles for both RM- and AM-based lenses should continuously vary from 0 to 2π , indicating that the curvature surface of the designed element must smoothly vary to yield the desired phase, resulting in extreme difficulty in fabrication. Optical metasurfaces,^[7–35] the 2D counterparts of metamaterials, have opened up new avenues in manipulating the phase, amplitude, and polarization of light at subwavelength resolution. Benefiting from the unprecedented ability to manipulate the electromagnetic wavefront and ease of fabrication,

1. Introduction

Traditional lenses are at a significant disadvantage in 3D scene imaging and 3D object imaging. Recently, lenses with an extended focal depth have attracted considerable attention owing to their practical applications in imaging with high axial and


a plethora of metalenses, such as dual-polarity plasmonic metalenses,^[36] multifoci lenses,^[37] multifunctional metalenses,^[38] broadband achromatic metalenses,^[39–41] and metalens arrays,^[42] with novel functions that are challenging to achieve by using traditional lenses have been proposed and realized. In addition to the traditional metalens with a limited focal depth, the light sword metasurface lens^[43] with an extended focal depth has been demonstrated. Although this approach tackles the technical challenge of fabrication of LSOEs, two intractable issues have to be urgently settled: (i) Metalenses have shown simultaneous extended focal depth and polarization-insensitive functionality. (ii) Imaging with high tolerance in the longitudinal direction has not yet been demonstrated. Although polarization-independent metalenses (with a limited focal range) have been demonstrated,^[44–46] they are limited to high structural complexity or lose a degree of freedom in the design space. Here, we propose an approach to realize a polarization-insensitive metalens with an extended focal depth using anisotropic dielectric micropillars (geometric metasurfaces). Unlike polarization-dependent LSOEs with AM,^[43] a polarization-insensitive terahertz (THz) AXL with RM is demonstrated in this paper. Under the illumination of arbitrarily polarized THz waves, this metalens shows a focal depth of $\approx 23\lambda$ along the propagation direction. Longitudinal high-tolerance imaging is experimentally demonstrated based on such a THz AXL. The polarization-insensitive metalens with a long focal depth may be of interest for a variety of practical applications, such as imaging, lithography, and detection.

Prof. X. F. Zang, Dr. W. W. Xu, Prof. M. Gu, Dr. B. S. Yao, Prof. L. Chen, Prof. Y. Peng, Prof. J. Y. Xie, Prof. Y. M. Zhu, Prof. S. L. Zhuang
Terahertz Technology Innovation Research Institute
and Shanghai Key Lab of Modern Optical System
University of Shanghai for Science and Technology
No. 516 JunGong Road, Shanghai 200093, China
E-mail: ymzhu@usst.edu.cn

Prof. X. F. Zang, Prof. L. Chen, Prof. Y. Peng, Prof. J. Y. Xie,
Prof. Y. M. Zhu
Shanghai Institute of Intelligent Science and Technology
Tongji University
Shanghai 200092, China

Prof. A. V. Balakin, Prof. A. P. Shkurinov
Department of Physics and International Laser Center
Lomonosov Moscow State University
Leninskie Gory 1, Moscow 19991, Russia

Prof. A. V. Balakin, Prof. A. P. Shkurinov
ILIT RAS – Branch of the FSRC «Crystallography and Photonics» RAS
Svyatozerskaya 1, Moscow Region 140700, Shatura, Russia

 The ORCID identification number(s) for the author(s) of this article can be found under <https://doi.org/10.1002/adom.201901342>.

DOI: 10.1002/adom.201901342

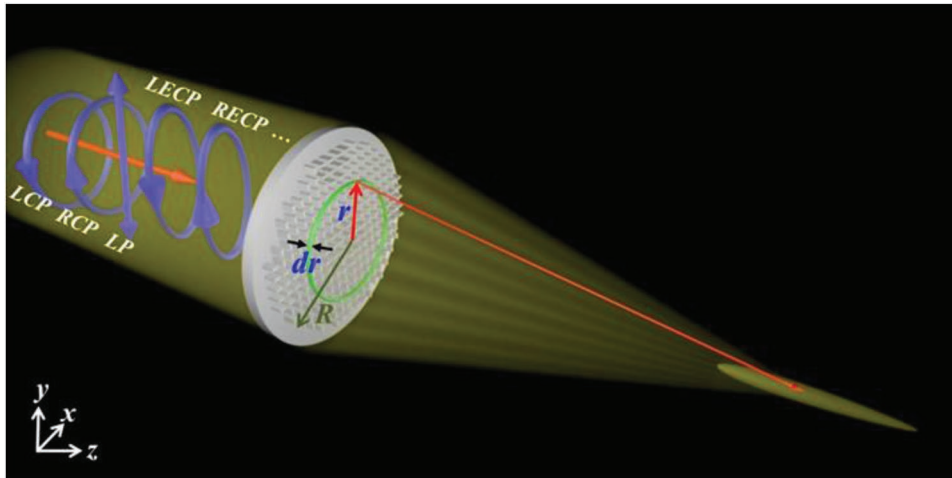


Figure 1. Schematic of the polarization-insensitive metacylinder with an extended focal depth. Under the illumination of arbitrarily polarized THz waves, a focal spot with the main electric field distributed from f to $f + \Delta f$ is observed. Each infinitesimal ring section of $2\pi r dr$ contributes to the focal length/region of $f + \Delta f \cdot r^2/R^2$.

2. Design and Methods

Figure 1 shows a schematic of a polarization-insensitive dielectric metacylinder (AXL) with an extended focal depth. When illuminated by arbitrarily polarized light beams, one focal spot with an extended focal depth is always observed after the metacylinder. Unlike with the traditional polarization-dependent metacylinders, incident light with an arbitrary polarization is consistently focused to a focal point, leading to a polarization-insensitive metacylinder. The key to realizing such a polarization-insensitive metacylinder is that a single metasurface can simultaneously focus both left-hand circularly polarized (LCP) and right-hand circularly polarized (RCP) light beams. An arbitrarily polarized light beam can be considered as a superposition of both LCP and RCP components with different amplitudes and a phase difference. Therefore, an arbitrarily polarized light beam can be focused to a focal point.

The phase profile of the AXL is defined by the following relation^[47–49]

$$\varphi(r) = \frac{k \cdot r^2}{2[f + (\Delta f \cdot r^2/R^2)]} \quad (1)$$

where r is the radial coordinate, and $k = 2\pi/\lambda$ is the free-space wave vector. λ is the wavelength of the incident light. f and Δf represent the focal length and the focal range of the metacylinder, respectively. R is the radius of the AXL. Equation (1) shows the radially symmetric phase modulation. Each infinitesimal ring section, i.e., $2\pi r dr$, contributes to the focal length/region of $f + \Delta f \cdot r^2/R^2$. According to Equation (1), the focal spot is stretched from f to $f + \Delta f$. If $\Delta f = 0$, then this equation reduces to a quadratic term $\left(\varphi(r) = \frac{k \cdot r^2}{2f}\right)$ ^[47,48] of the spherical phase of $\varphi(r) = k \cdot \sqrt{r^2 + f^2}$.

For a geometric metasurface, the phase profile of Equation (1) can be realized for helicity-dependent light incidence, i.e., focusing LCP light and defocusing the opposite helicity.

Under the illumination of LCP light, the transmitted focal light field can be written as a Jones vector

$$E_{\text{RCP}} = \eta(\lambda) \begin{bmatrix} 1 \\ -i \end{bmatrix} \exp(i\varphi(r)) \quad (2)$$

where $\eta(\lambda)$ is the conversion efficiency.

To break the helicity-dependent limitation, an additional phase of $\varphi'(r) = -\varphi(r) = -\frac{k \cdot r^2}{2[f + (\Delta f \cdot r^2/R^2)]}$ is introduced to focus the light with opposite helicity. An arbitrarily polarized light beam can be decomposed into a superposition of LCP and RCP components with different amplitudes and a phase difference. The Jones vector is as follows

$$E_{\text{arbitrary}} = A \begin{bmatrix} 1 \\ -i \end{bmatrix} + B e^{i\alpha} \begin{bmatrix} 1 \\ i \end{bmatrix} \quad (3)$$

where A and B are the scale coefficients of amplitude, with $|A|^2 + |B|^2 = 1$. α is the phase difference between the LCP and RCP components, and it can be merged into coefficient B (since α is not related to the geometric phases $\varphi(r)$ and $\varphi'(r)$),

with the formula $E_{\text{arbitrary}} = A \begin{bmatrix} 1 \\ -i \end{bmatrix} + B' \begin{bmatrix} 1 \\ i \end{bmatrix}$. Therefore, under the illumination of an arbitrarily polarized light beam, the corresponding Jones vector of the transmitted light field can be described as

$$E_{\text{transmitted}} = \frac{1}{\sqrt{2}} \left\{ A \cdot \eta(\lambda) \begin{bmatrix} 1 \\ i \end{bmatrix} \exp(i\varphi(r)) + A \cdot \eta(\lambda) \begin{bmatrix} 1 \\ i \end{bmatrix} \exp(-i\varphi(r)) \right\} + \frac{1}{\sqrt{2}} \left\{ B' \cdot \eta(\lambda) \begin{bmatrix} 1 \\ -i \end{bmatrix} \exp(-i\varphi(r)) + B' \cdot \eta(\lambda) \begin{bmatrix} 1 \\ -i \end{bmatrix} \exp(i\varphi(r)) \right\} \quad (4)$$

Both the LCP and RCP components are associated with the two parameters $\exp(i\varphi(r))$ and $\exp(-i\varphi(r))$, and the total phase

profile for the metalens with an extended focal depth (see the schematic of Figure 1) can be described as

$$\Phi(r) = \arg \left\{ \exp[i\varphi(r)] + \exp[-i\varphi(r)] \right\} \quad (5)$$

Here, $\varphi(r)$ is one phase profile for focusing LCP incident THz waves, and $-\varphi(r)$ is the other phase profile for focusing RCP incident THz waves (vice versa). When LCP (RCP) THz waves pass through a micropillar, the transmitted electric field of converted (RCP (LCP)) THz waves can be described as $A \cdot \exp^{\pm 2\alpha} \begin{bmatrix} 1 \\ \pm i \end{bmatrix}$. A represents the complex transmission coefficient, and α is the counterclockwise rotation angle of the pillar with respect to the x -axis. For $\alpha \neq 0^\circ, 90^\circ$, the converted THz waves (both LCP and RCP THz waves) will experience different phase profiles ($\pm 2\alpha$), leading to a polarization-sensitive phase profile (or polarization-dependent metalens). When $\alpha = 0^\circ$ or $\alpha = 90^\circ$, the values of $\exp^{2\alpha}$ and $\exp^{-2\alpha}$ become equal, meaning that both LCP and RCP incident THz waves will experience the same phase profile. An arbitrarily polarized THz beam can be decomposed into a superposition of LCP and RCP components, and thus, the arbitrarily polarized THz beam will experience the same phase profile for $\alpha = 0^\circ$ or $\alpha = 90^\circ$, resulting in a polarization-insensitive metalens. In addition, Equation (5) consists of the

phase profile of a convex lens and a concave lens (resulting in a diverging beam). Under the illumination of LCP (or RCP) THz waves, no more than half (50%) of the transmitted waves will be converted to RCP (or LCP) light (for focusing). Therefore, the theoretical limit of the focusing efficiency for the designed metalens cannot exceed 50%.

To realize a polarization-insensitive metalens with an extended focal depth, a dielectric metasurface consisting of anisotropic silicon micropillars is designed, as shown in Figure 2a. The design parameters of each micropillar are $L = 85 \mu\text{m}$, $W = 40 \mu\text{m}$, and $H = 500 \mu\text{m}$. The unit cell period is $p = 110 \mu\text{m}$ along both the x - and y -axes. The design of the silicon pillars is shown in Ref. [50], and the polarization conversion efficiency of the unit cell is given in Section S1 in the Supporting Information. The standard photolithography technology and DRIE (Bosch) process are applied to fabricate the metalens. Figure 2b shows optical images of the sample used to generate a polarization-insensitive focal point with an extended focal depth. We experimentally demonstrate the characteristics of the metalens and longitudinal high-tolerance imaging using near-field scanning terahertz microscopy (NSTM), as shown in Figure 2c. The THz tip is utilized to correct the field distribution. The detailed measurement method is given in the Experimental Section.

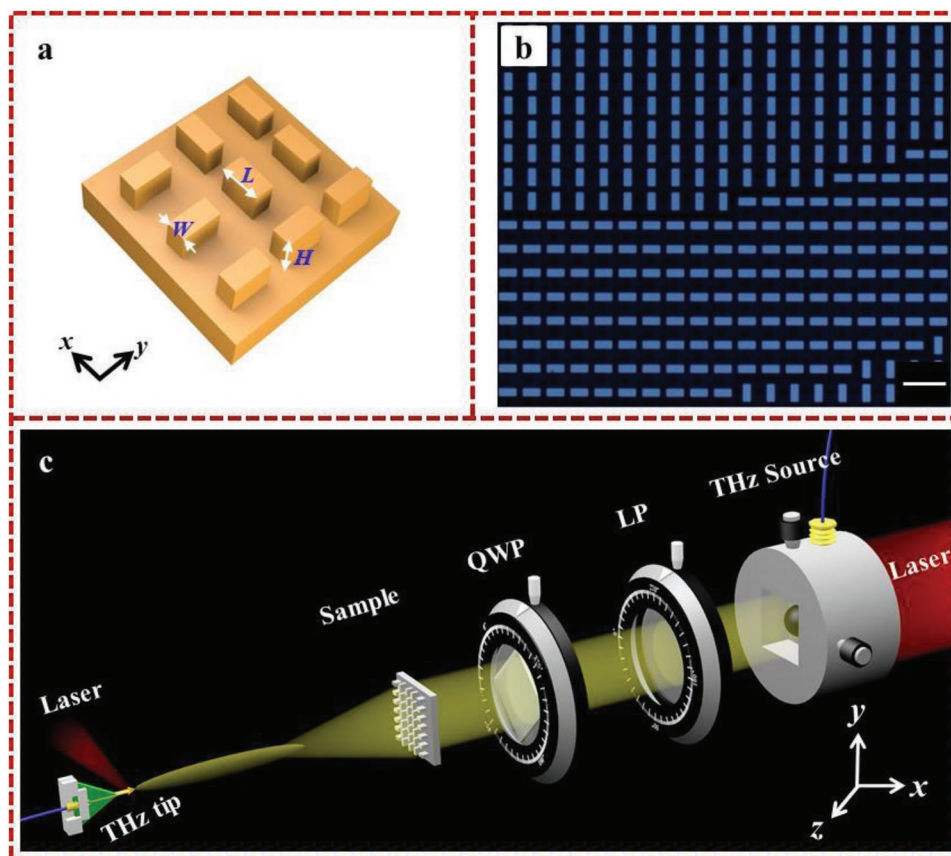


Figure 2. Design and fabrication of the metasurface and schematic of the experimental setup. a) Illustration of the metasurface with micropillars deposited on a silicon substrate. b) Optical image of the fabricated metalens for generating a focal spot with an extended focal depth. The scale bar is 200 μm . c) Schematic of the experimental setup.

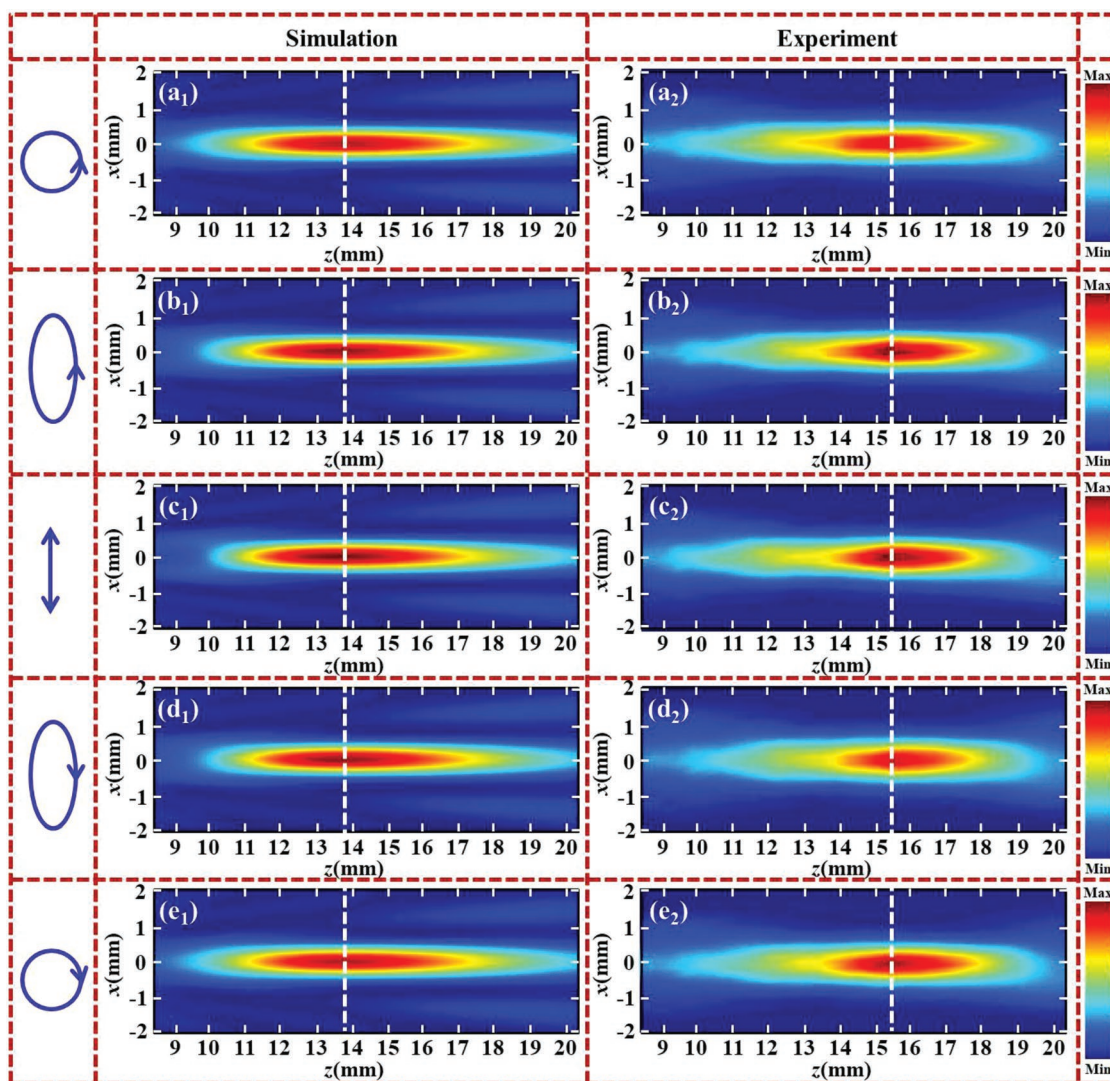


Figure 3. Electric field distributions for the metalens with an extended focal depth. a_1 – e_1) Simulated electric field distributions for the transmitted THz waves in the x – z plane under the illumination of THz waves with the polarization switched from LCP to RCP. a_2 – e_2) Corresponding experimental results.

3. Results and Discussions

Figure 3 shows numerical simulations and experimental demonstrations of the polarization-insensitive metalens with an extended focal depth. Here, the THz metalens consists of 100×100 micropillars with different rotation orientations to yield the desired phase (see the phase profile in Equation (5)). The focusing parameters are designed as: $f = 10$ mm and $\Delta f = 10$ mm, which means that a focal spot with the main power is focused in the region between 10 and 20 mm from the sample. The working frequency is selected as 0.69 THz. The finite difference time domain method is utilized to calculate the field distribution of the designed metalens under the illumination of arbitrarily polarized THz waves. Figure 3 a_1 illustrates the electric field distribution after LCP THz waves pass through such a metalens at normal incidence. A focal spot with the main field distribution ranging from 10 to 20 mm is clearly observed, which agrees well with the designed

focal length. The center (maximum value) of the focal spot is located at $z = 13.9$ mm (see the white line in the left column of Figure 3). In Figure 3 b_1 – e_1 , we show the cases of illumination under LECP (left-hand elliptically polarized), LP (linearly-polarized), RECP (right-hand elliptically polarized), and RCP THz waves. All of the calculated electric field distributions demonstrate that one focal spot with an extended focal depth is always observed after the metalens under the illumination of arbitrarily polarized THz waves. Figure 3 a_2 – e_2 shows the corresponding experimental results. All of the foci are mainly distributed from 10 to 19.6 mm, showing good consistency with the theoretical design. The center of the focal spots in the experiment is located at $z = 15.5$ mm (see the white line in the right column of Figure 3), which deviates from the calculations, with a relative displacement of 1.6 mm. The field distributions for both the calculated and experimental results match each other well except for a slight discrepancy, i.e., different center positions and focal depths, which may be caused by fabrication

errors and the measurement accuracy. The focusing efficiency (under the illumination of arbitrarily polarized THz waves) in the simulation is approximately 35%, while it is 23.8%, 25.4%, 26.1%, 24.9%, and 25.1% (in the experiments) for the LCP, LECP, LP, RECP, and RCP THz waves. The electric field distributions of the focal spot in the y - z plane are investigated and supplied in Section S2 in the Supporting Information. The measurement method for the focusing efficiency is given in Section S3 in the Supporting Information.

To analyze the polarization-insensitive characteristic of the metalens, the field/intensity distribution at the center of each focal spot is shown in **Figure 4**. The calculated electric field distributions in the x - y plane (at $z = 13.9$ mm) are shown in Figure 4a₁-e₁. For the illumination of THz waves with the polarization switching from LCP to RCP, the field distributions ($z = 13.9$ mm) of the focal spots are nearly identical. The experimental measurements for the metalens at $z = 15.5$ mm are shown in Figure 4a₂-e₂, where the corresponding field distributions are also nearly the same. The normalized intensity along $y = 0$ is illustrated in Figure 4a₃-e₃. The normalized intensities at $z = 13.9$ mm (red lines for simulations) (or $z = 15.5$ mm (blue lines for measurements)) exhibit almost no change under polarization switching, demonstrating polarization insensitivity. The field/intensity distributions at $z = 12$ mm and $z = 18.5$ mm are experimentally demonstrated in Section S4 in the Supporting Information.

To further characterize the metalens with a mathematical transformation ($\Delta f = 10$ mm), high-tolerance imaging in the longitudinal direction is demonstrated based on the designed AXL. As a comparison, the metalens without a mathematical transformation ($\Delta f = 10$ mm) is fabricated, and the measured field distribution under the illumination of LP THz waves is shown in **Figure 5a**. The focal spot is mainly distributed from 8.3 to 12.4 mm (with a focal depth of 4.1 mm). An arrow-shaped sample consisting of metal slits is designed for imaging, as shown in Figure 5c,d. The numerical simulations of the transmission characteristics for the metal slits are supplied in Section S3 in the Supporting Information. Under the illumination of y -polarized THz waves, an arrow is revealed, whereas nothing can be observed for the x -polarized THz wave (see Figure 5c,d and Section S5 in the Supporting Information). In the experiment, the arrow-shaped sample is located at three different positions (see the white dotted lines in Figure 5a,b) of the focal spot for imaging. The distance between two neighboring white dotted lines (see Figure 5a,b) is $d = 4$ mm. For imaging, the positions of the metalens and THz tip are fixed, and the arrow-shaped sample is scanned in the x - y plane to reveal the desired imaging. Figure 5e₁-e₃ shows the imaging results obtained using the traditional lens (see Figure 5a) when the arrow-shaped sample is placed at $z = 6$ mm, $z = 10$ mm, and $z = 14$ mm. **The arrow is observed at $z = 10$ mm, while it cannot be revealed at $z = 6$ mm, and $z = 14$ mm.** However, **for the AXL, the arrow is observed at $z = 11$ mm, $z = 15$ mm, and $z = 19$ mm, as shown in Figure 5f₁-f₃, demonstrating high-tolerance imaging in the longitudinal direction.** In other words, the focal depth of the metalens with $\Delta f = 10$ mm is indeed longer than that in the case of $\Delta f = 0$. The imaging based on the AXL under the illumination of LCP, LECP, RECP, and RCP THz waves is shown in Section S6 in the Supporting Information.

A comparison between the metalens with an extended focal depth and the traditional metalens with the same effective focal length is given in Section S7 in the Supporting Information.

The approach to designing polarization-insensitive geometric metasurfaces using anisotropic metal/dielectric pillars is highly desirable and can enable the realization of efficient functional (polarization-insensitive) metalenses with additional degrees of freedom, i.e., by rotating the pillars to generate the Pancharatnam-Berry phase, to control the wavefront of electromagnetic waves. Although the traditional symmetric cylindrical or square-shaped pillars overcome the challenge of polarization sensitivity, they lose a degree of freedom in the design space due to the symmetry of the structures, resulting in the metasurfaces suffering from geometric complexity. In this work, we demonstrated a unique approach to realizing a polarization-insensitive metalens (using anisotropic dielectric micropillars) with a focal depth of $\approx 23\lambda$ along the propagation direction under the illumination of arbitrarily polarized THz waves, leading to a polarization-insensitive metalens with an extended focal depth. Such a focal spot (with an extended focal depth) enables applications in longitudinal high-tolerance imaging in the THz region, which has not yet been demonstrated. The polarization-insensitive metalens with an extended focal depth has unusual functions, i.e., an ultralong focusing region and imaging with high tolerance in the longitudinal direction, which are unique and very difficult to achieve with conventional lenses.

4. Conclusion

In summary, we have proposed an approach to designing a polarization-insensitive metalens with an extended focal depth using anisotropic dielectric micropillars. A focal spot with an ultralong focusing distance ranging from 10 to 19.6 mm is experimentally demonstrated under the illumination of arbitrarily polarized THz waves. Benefiting from the metalens with an extended focal depth, THz high-tolerance imaging in the longitudinal direction is realized. Our unique approach to focal depth manipulation and high-tolerance long-range imaging may find a variety of applications in imaging, lithography and information processing.

5. Experimental Section

Sample Fabrication: Standard photolithography, the DRIE (Bosch) process and magnetron sputtering coating were utilized to fabricate the metalens and arrow-shaped imaging sample. For the metalens, an AZP4620 image reversal photoresist layer with a thickness of 7–8 μm was spin-coated onto a high resistivity silicon wafer. The micropillars were patterned by standard photolithography. Then, the metalens was fabricated based on DRIE etching for a proper time. For the arrow-shaped imaging sample, the arrow pattern coated on a PI (polyimide) film (substrate) was also formed based on traditional photolithography. In addition to DRIE etching, magnetron sputtering coating and ultrasonic stripping were also used to fabricate gold arrays (arrow-shaped sample) in the metal coating.

Experimental Setup: The NSTM system shown in Figure 2c was built to characterize the performance of the metalens and imaging. A femtosecond laser pulse with a central wavelength of 780 nm was split into two parts: one of the beams was focused onto the THz antenna

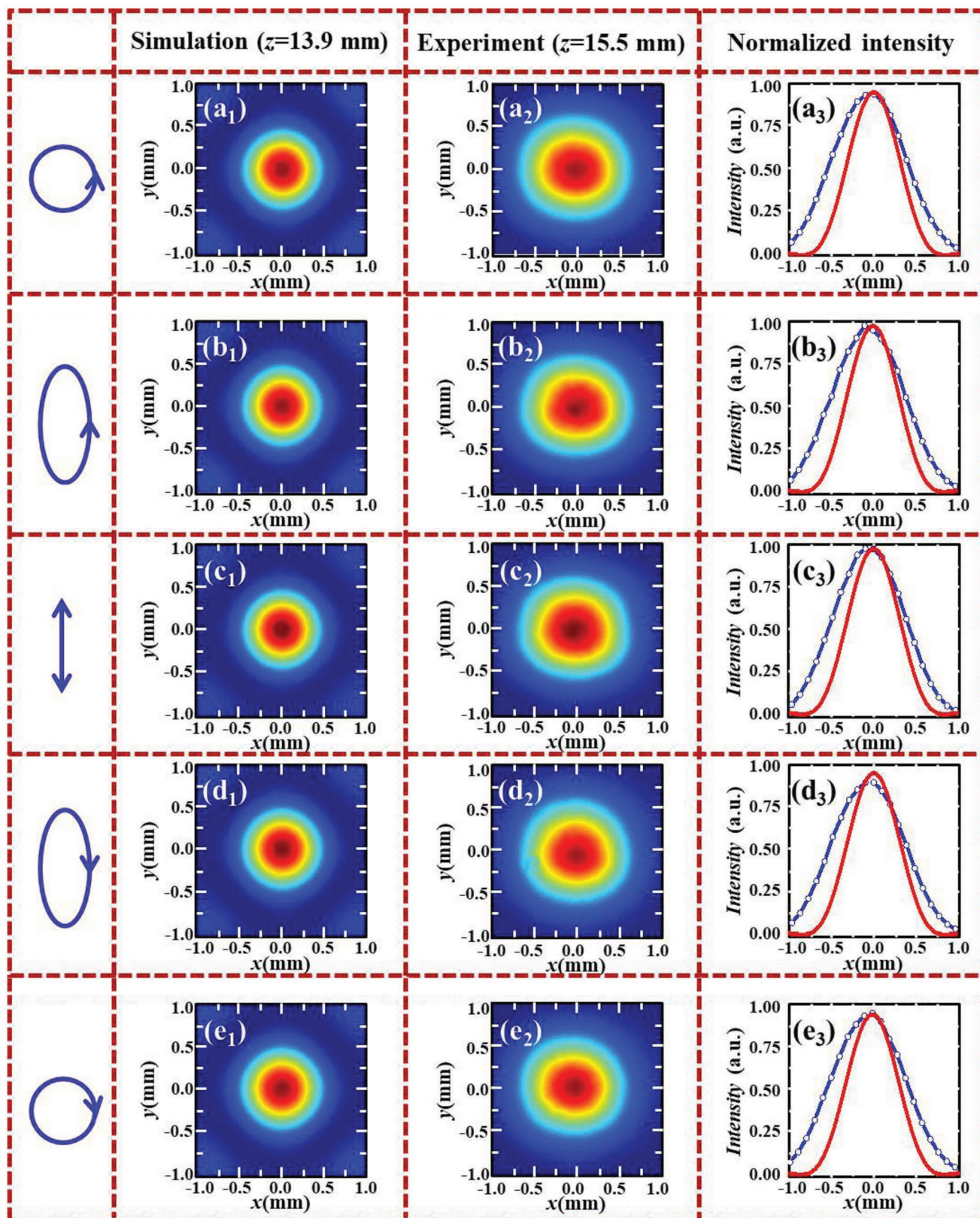


Figure 4. Electric field distributions for the metalelens with an extended focal depth. a_1 – e_1) Simulated y - and x -polarized electric field distributions for the transmitted THz waves in the x - y plane under the illumination of THz waves with the polarization switched from LCP to RCP. a_2 – e_2) Corresponding experimental results. a_3 – e_3) Normalized intensity at $y = 0$ with red lines for simulations and blue lines for measurements.

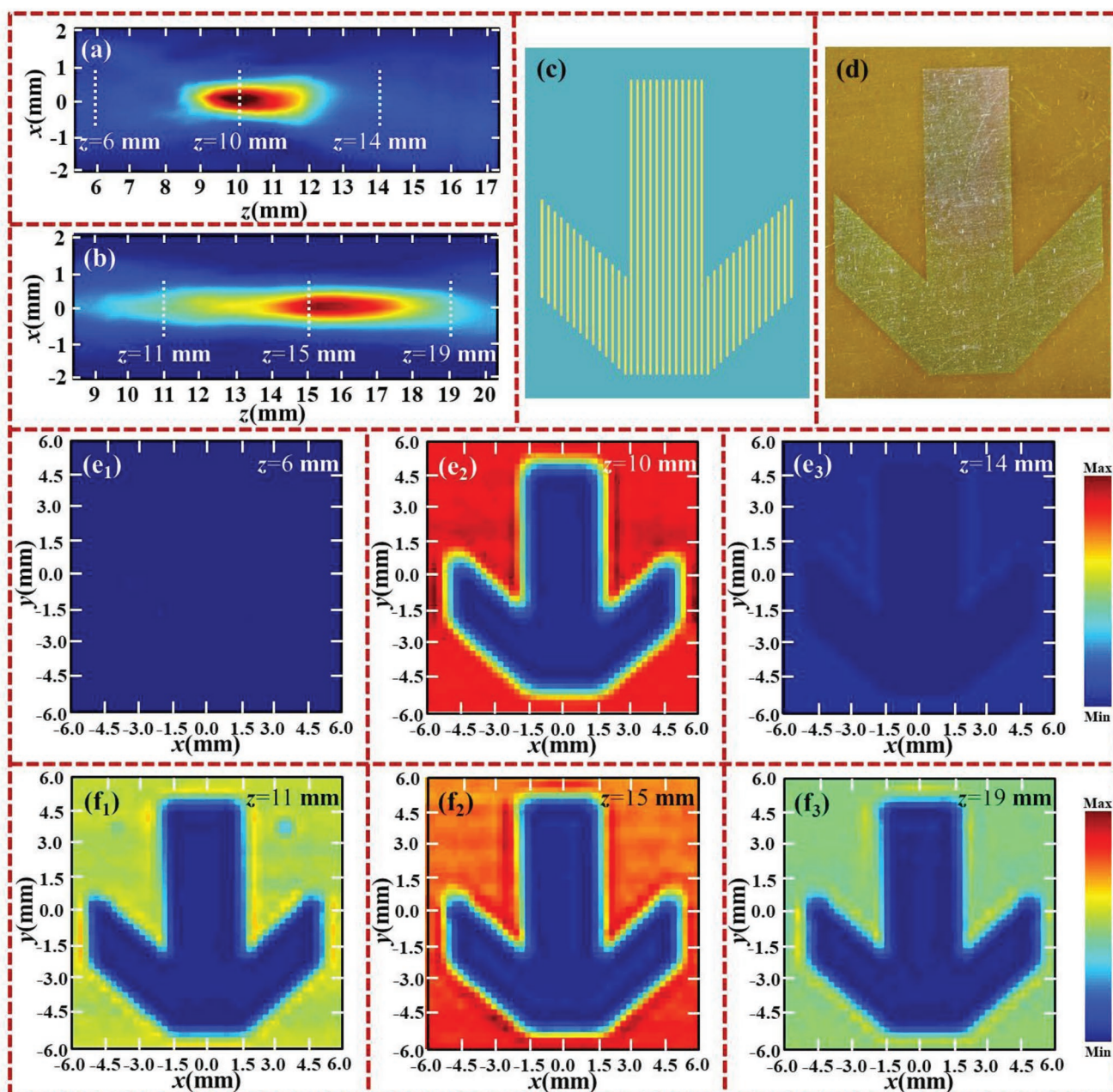


Figure 5. Longitudinal long-range imaging. a,b) Electric field distributions for the metalenses (with $\Delta f = 0$ for panel (a) and $\Delta f = 10$ mm for panel (b)) under the illumination of LP THz waves. c,d) Schematic and optical image of the designed arrow-shaped sample. e₁–e₃) Measured images (for the metalens with $\Delta f = 0$) with the designed imaging sample located at $z = 6$ mm, $z = 10$ mm, and $z = 14$ mm. f₁–f₃) Measured images (for the metalens with $\Delta f = 10$ mm) with the designed imaging sample located at $z = 11$ mm, $z = 15$ mm, and $z = 19$ mm. The scale bar is 2 mm.

to generate the THz radiation, while the other beam was coupled into a single-mode fiber (with a length of 10 cm) and guided onto the THz tip to induce photon-generated carriers for detection. The THz waves impinged on the metalens/imaging sample, and the THz tip mounted on a 3D translation stage was located behind the sample to record the electric field. The electric field distributions of the focal spot and imaging were revealed by scanning/shifting the THz tip or imaging sample, respectively. In the experiment, the electric field was detected at a 100 μm step in both the x-direction and y-direction and at a 200 μm step along the z-direction.

Supporting Information

Supporting Information is available from the Wiley Online Library or from the author.

Acknowledgements

This work is supported in part by the Major National Development Project of Scientific Instrument and Equipment (2016YFF0100503), National

Key Research and Development Program of China (2017YFA0701005), National Natural Science Foundation of China (61871268, 61722111, 61705131), Natural Science Foundation of Shanghai (18ZR1425600), Shanghai Pujiang Program (18PJD033), “Shuguang” Program of Shanghai Education Commission (19SG44), Shanghai international joint laboratory project (17590750300), 111 Project (D18014), Science and technology development project of USST (2018KJFZ087), and State Key Laboratory of Advanced Optical Communication Systems and Networks, Shanghai Jiao Tong University, China (2018GZKF03004). We thank Prof. Xianzhong Chen (Heriot-Watt University) for helpful suggestions.

Conflict of Interest

The authors declare no conflict of interest.

Author Contributions

X.F.Z. and Y.M.Z. initiated the idea. W.W.X. and X.F.Z. conducted the numerical simulations. W.W.X. and B.S.Y. performed the measurements. X.F.Z., W.W.X., M.G., B.S.Y., L.C., Y.P., J.Y.X., A.V.B., A.P.S., Y.M.Z., and S.L.Z. prepared the manuscript. X.F.Z. and Y.M.Z. supervised the project. All the authors discussed and analyzed the results.

Keywords

beam manipulation, geometric phase, high-tolerance imaging, THz metalems

Received: August 6, 2019

Revised: October 4, 2019

Published online:

- [1] B. Z. Dong, G. Z. Yang, B. Y. Gu, *J. Opt. Soc. Am. A* **1996**, *13*, 97.
- [2] J. S. Ye, B. Z. Dong, B. Y. Gu, G. Z. Yang, S. T. Liu, *J. Opt. Soc. Am. A* **2002**, *19*, 2030.
- [3] F. Qin, K. Huang, J. Wu, J. Teng, C. W. Qiu, M. H. Hong, *Adv. Mater.* **2017**, *29*, 1602721.
- [4] K. Petelczyc, S. Bara, A. C. Lopez, Z. Jaroszewicz, K. Kakarenko, A. Kolodziejczyk, M. Sypek, *Opt. Express* **2011**, *19*, 25602.
- [5] K. Kakarenko, I. Ducin, K. Grabowiecki, Z. Jaroszewicz, A. Kolodziejczyk, A. Mira-Agudelo, K. Petelczyc, A. Skladowska, M. Sypek, *Biomed. Opt. Express* **2015**, *6*, 1738.
- [6] G. Mikula, Z. Jaroszewicz, A. Kolodziejczyk, K. Petelczyc, M. Sypek, *Opt. Express* **2007**, *15*, 9184.
- [7] N. Yu, P. Genevet, M. A. Kats, F. Aieta, J.-P. Tetienne, F. Capasso, Z. Gaburro, *Science* **2011**, *334*, 333.
- [8] L. Huang, X. Chen, H. Mühlenbernd, G. Li, B. Bai, Q. Tan, G. Jin, T. Zentgraf, S. Zhang, *Nano Lett.* **2012**, *12*, 5750.
- [9] X. J. Ni, N. K. Emani, A. V. Kildishev, A. Boltasseva, V. M. Shalaev, *Science* **2012**, *335*, 427.
- [10] S. L. Sun, Q. He, S. Y. Xiao, Q. Xu, X. Li, L. Zhou, *Nat. Mater.* **2012**, *11*, 426.
- [11] X. Yin, Z. Ye, J. Rho, Y. Wang, X. Zhang, *Science* **2013**, *339*, 1405.
- [12] X. Luo, *Sci. China: Phys., Mech. Astron.* **2012**, *58*, 594201.
- [13] N. Grady, J. Heyes, D. Chowdhury, Y. Zeng, M. Reiten, A. Azad, A. Taylor, D. Dalvit, H. Chen, *Science* **2013**, *340*, 1304.
- [14] G. Zheng, H. Mühlenbernd, M. Kenney, G. Li, T. Zentgraf, S. Zhang, *Nat. Nanotechnol.* **2015**, *10*, 308.
- [15] D. Wen, F. Yue, G. Li, G. Zheng, K. Chan, S. Chen, M. Chen, K. F. Li, P. W. H. Wong, K. W. Cheah, E. Yue Bun Pun, S. Zhang, X. Chen, *Nat. Commun.* **2015**, *6*, 8241.
- [16] Y. W. Huang, W. T. Chen, W. T. W. Y. Tsai, P. C. Wu, C. M. Wang, G. Sun, D. P. Tsai, *Nano Lett.* **2015**, *15*, 3122.
- [17] W. Ye, F. Zeuner, X. Li, B. Reineke, S. He, C. Qiu, J. Liu, Y. Wang, S. Zhang, T. Zentgraf, *Nat. Commun.* **2016**, *7*, 11930.
- [18] F. Zhang, M. Pu, X. Li, P. Gao, X. Ma, J. Luo, H. Yu, X. Luo, *Adv. Funct. Mater.* **2017**, *27*, 1704295.
- [19] A. Arbabi, Y. Horie, M. Bagheri, A. Faraon, *Nat. Nanotechnol.* **2015**, *10*, 937.
- [20] M. Pu, X. Li, X. Ma, Y. Wang, Z. Zhao, C. Wang, C. Hu, P. Gao, C. Huang, H. Ren, X. Li, F. Qin, J. Yang, M. Gu, M. Hong, X. Luo, *Sci. Adv.* **2015**, *1*, e1500396.
- [21] X. Li, L. Chen, Y. Li, X. Zhang, M. Pu, Z. Zhao, X. Ma, Y. Wang, M. Hong, X. Luo, *Sci. Adv.* **2016**, *2*, e1601102.
- [22] B. Wang, F. L. Dong, Q. T. Li, D. Yang, C. W. Sun, J. J. Chen, Z. W. Song, L. H. Xu, W. G. Chu, Y. F. Xiao, Q. H. Gong, Y. Li, *Nano Lett.* **2016**, *16*, 5235.
- [23] B. H. Chen, P. C. Wu, V.-C. Su, Y.-C. Lai, C. H. Chu, I. C. Lee, J.-W. Chen, Y. H. Chen, Y. C. Lan, C. H. Kuan, D. P. Tsai, *Nano Lett.* **2017**, *17*, 6345.
- [24] L. Jin, Z. Dong, S. Mei, Y. F. Yu, Z. Wei, Z. Pan, S. D. Rezaei, X. Li, A. I. Kuznetsov, Y. S. Kivshar, J. K. W. Yang, C.-W. Qiu, *Nano Lett.* **2018**, *18*, 8016.
- [25] X. F. Zang, F. L. Dong, F. Y. Yue, C. M. Zhang, L. H. Xu, Z. W. Song, M. Chen, P. Y. Chen, G. S. Buller, Y. M. Zhu, S. L. Zhuang, W. G. Chu, S. Zhang, X. Z. Chen, *Adv. Mater.* **2018**, *30*, 1707499.
- [26] X. F. Zang, H. H. Gong, Z. Li, J. Y. Xie, Q. Q. Cheng, L. Chen, A. P. Shkurinov, Y. M. Zhu, S. L. Zhuang, *Appl. Phys. Lett.* **2018**, *112*, 171111.
- [27] M. Mehmood, S. Mei, S. Hussain, K. Huang, S. Siew, L. Zhang, T. Zhang, X. Ling, H. Liu, J. Teng, A. Danner, S. Zhang, C. W. Qiu, *Adv. Mater.* **2016**, *28*, 2533.
- [28] F. Y. Yue, D. D. Wen, C. M. Zhang, B. D. Gerardot, W. Wang, S. Zhang, X. Z. Chen, *Adv. Mater.* **2017**, *29*, 1603838.
- [29] X. F. Zang, Y. M. Zhu, C. X. Mao, W. W. Xu, H. Z. Ding, J. Y. Xie, Q. Q. Cheng, L. Chen, Y. Peng, Q. Hu, M. Gu, S. L. Zhuang, *Adv. Opt. Mater.* **2019**, *7*, 1801328.
- [30] G. Li, M. Kang, S. M. Chen, S. Zhang, E. Y.-B. Pun, K. W. Cheah, J. Li, *Nano Lett.* **2013**, *13*, 4148.
- [31] X. H. Ling, X. X. Zhou, X. N. Yi, W. X. Sun, Y. C. Liu, S. Z. Chen, H. L. Luo, D. Y. Fan, *Light: Sci. Appl.* **2015**, *4*, e290.
- [32] W. Luo, S. Xiao, Q. He, S. Sun, L. Zhou, *Adv. Opt. Mater.* **2015**, *3*, 1102.
- [33] A. Shaltout, J. J. Liu, A. Kildishev, V. Shalaev, *Optica* **2015**, *2*, 860.
- [34] J. Zhou, H. Qian, G. Hu, H. Luo, S. Wen, Z. Liu, *ACS Nano* **2018**, *12*, 82.
- [35] X. F. Zang, C. X. Mao, X. G. Guo, G. J. You, H. Yang, L. Chen, Y. M. Zhu, S. L. Zhuang, *Appl. Phys. Lett.* **2018**, *113*, 071102.
- [36] X. Chen, L. Huang, H. Mühlenbernd, G. Li, B. Bai, Q. Tan, G. Jin, C. Qiu, S. Zhang, T. Zentgraf, *Nat. Commun.* **2012**, *3*, 1198.
- [37] X. Chen, M. Chen, M. Mehmood, D. Wen, F. Yue, C. Qiu, S. Zhang, *Adv. Opt. Mater.* **2015**, *3*, 1201.
- [38] D. Wen, F. Yue, M. Ardrón, X. Chen, *Sci. Rep.* **2016**, *6*, 27628.
- [39] A. Arbabi, Y. Horie, A. J. Ball, A. Faraon, *Nat. Commun.* **2015**, *6*, 7069.
- [40] R. Paniagua-Domínguez, Y. Yu, E. Khaidarov, S. Choi, V. Leong, R. M. Bakker, X. Liang, Y. Fu, V. Valuckas, L. A. Krivitsky, A. I. Kuznetsov, *Nano Lett.* **2018**, *18*, 2124.
- [41] S. Wang, P. Wu, V. Su, Y. Lai, M. Chen, H. Kuo, B. Chen, Y. Chen, T. Huang, J. Wang, R. Lin, C. Kuan, T. Li, Z. Wang, S. Zhu, D. Tsai, *Nat. Nanotechnol.* **2018**, *13*, 227.
- [42] R. Lin, V. Su, S. Wang, M. Chen, T. Chung, Y. Chen, H. Kuo, J. Chen, Y. Huang, J. Wang, C. Chen, P. Wu, T. Li, Z. Wang, S. Zhu, D. Tsai, *Nat. Nanotechnol.* **2019**, *14*, 227.
- [43] Z. Zhang, D. Wen, C. Zhang, M. Chen, W. Wang, S. Chen, X. Chen, *ACS Photonics* **2018**, *5*, 1794.

- [44] M. Khorasaninejad, A. Y. Zhu, C. Roques-Carmes, W. Chen, J. Oh, I. Mishra, R. C. Devlin, F. Capasso, *Nano Lett.* **2016**, *16*, 7229.
- [45] E. Arbabi, A. Arbabi, S. M. Kamali, Y. Horie, A. Faraon, *Optica* **2016**, *3*, 628.
- [46] W. Chen, A. Y. Zhu, J. Sisler, Z. Bharwani, F. Capasso, *Nat. Commun.* **2019**, *10*, 355.
- [47] N. Davidson, A. Friesem, E. Hasman, *Opt. Lett.* **1991**, *16*, 523.
- [48] J. Sochacki, S. Bara, Z. Jaroszewicz, A. Kolodziejczyk, *Opt. Lett.* **1992**, *17*, 7.
- [49] F. Diaz, F. Goudail, B. Loiseaux, J. Huignard, *Opt. Lett.* **2009**, *34*, 1171.
- [50] X. Zang, H. Ding, Y. Intaravanne, L. Chen, Y. Peng, J. Xie, Q. Ke, A. V. Balakin, A. P. Shkurinov, X. Chen, Y. Zhu, S. Zhuang. *Laser Photon. Rev.* **2019**, *13*, 1900182.